Plasmonics
https://doi.org/10.1007/s11468-025-03311-x

RESEARCH

Enhancement Factors of SERS Substrates Based on Monometallic and Bimetallic Nanoparticles Embedded on Reduced Graphene Oxide

Nashmitta Pillai[1] · Liyana Shatar[1] · Fatin H. Mustafa[2] · Muhammad S.A. Aziz[3] · Ali A. Alwahib[4,5] · Yasmin M. Kamil[6] · Fariza H. Suhailin[1,3]

Received: 18 July 2025 / Accepted: 21 October 2025

Abstract

This study presents a comparison of the enhancement factor (EF) of surface enhanced Raman scattering (SERS) substrates based on monometallic gold (Au), silver (Ag) and bimetallic gold-silver (Au-Ag) nanoparticles (NPs) embedded on reduced graphene oxide (rGO). The graphene oxide (GO) was synthesized via a modified Hummer's method and thermally reduced to form rGO. The NPs (Au, Ag and Au-Ag) were chemically synthesized via a bottom-up method and combined with rGO to form nanocomposites. The Au, Ag and Au–Ag bimetallic NPs exhibited surface plasmon resonance (SPR) peaks at 522, 384 and 415 nm, respectively, reflecting the influence of composition and alloying. Structural and morphological analysis revealed face-centered cubic NPs with lattice fringes and spherical shape, while rGO displayed a wrinkled sheet-like morphology, providing a high surface area for NPs attachment. The SERS performance was evaluated using rhodamine 6G (R6G) as a Raman reporter to calculate the enhancement factor (EF). The bimetallic Au-Ag/rGO substrate exhibited an EF of 1.12×10^8, significantly 4 times higher than Au/rGO (2.70×10^7) and 2 times higher than Ag/rGO (4.92×10^7), with detection limit of R6G as low as 10^{-10} M. This enhancement was attributed to the synergistic plasmonic coupling between Au and Ag, which generated stronger localized electromagnetic fields and increased hotspot density. These observations signify the potential of the bimetallic Au-Ag/rGO SERS substrate over the monometallic NPs for practical applications.

Keywords SERS · Enhancement factor · Metallic nanoparticles · Reduced graphene oxide

Introduction

Surface enhanced Raman spectroscopy (SERS) is a technique that amplifies Raman scattering signals of molecules adsorbed on nanostructured metallic surfaces. The enhancement in SERS results from two primary mechanisms, which are the electromagnetic (EM) mechanism and chemical (CM) mechanism [1, 2]. The EM mechanism is the dominant contributor and arises from localized surface plasmon resonance (LSPR) in noble metal NPs. LSPR occurs when incident light excites collective oscillation of conduction electrons, generating strongly localized EM fields. These fields are significantly amplified at hotspots, which are regions of high field intensity between neighboring NPs [3]. Conversely, the CM mechanism originates from charge transfer between the analyte and the substrate surface, altering the molecule's polarizability and enhancing Raman scattering. The degree of signal enhancement is measured by enhancement factor (EF), which quantifies amplification

✉ Fariza H. Suhailin
farizahanim@utm.my

1 Department of Physics, Faculty of Science, Universiti Teknologi Malaysia, 81310 Skudai, Johor Bahru, Malaysia

2 Department of Electronic and Computer Engineering, Faculty of Electrical Engineering, Universiti Teknologi Malaysia, 81310 Skudai, Johor Bahru, Malaysia

3 Laser Center, Ibnu Sina Institute for Scientific and Industrial Research (ISI-SIR), Universiti Teknologi Malaysia, 81310 Skudai, Johor Bahru, Malaysia

4 Wireless and Photonic Networks Research Centre, Faculty of Engineering, Universiti Putra Malaysia, 43400 Serdang, Selangor, Malaysia

5 Department of Laser and Optoelectronics Engineering, University of Technology, Baghdad, Iraq

6 Department of Microbiology, Faculty of Biotechnology and Biomolecular Science, Universiti Putra Malaysia, 43400 Serdang, Selangor, Malaysia

Published online: 10 November 2025

relative to standard Raman scattering [4]. Recent studies have reported typical EF values ranging from 10^6 to 10^{11} for various SERS substrates, depending on substrate design and analyte type [5–7]. The ability to amplify Raman signals through controlled plasmonic interactions has positioned SERS as a valuable tool for trace detection, even at the single-molecule level.

The size, shape, composition and spatial arrangement of nanostructures influence SERS enhancement. For instance, smaller nanoparticles (NPs) or optimized NP arrays can promote stronger plasmonic coupling, resulting in higher hotspots density and more consistent signal amplification. Anisotropic NPs, such as nanostars (NSs) and nanorods (NRs), exhibit sharp features and strong plasmonic effects, while nanospheres provide advantages in uniformity and reproducibility [8]. By facilitating the formation of localized EM hotspots, nanospheres can achieve reliable EF values, making them highly effective for SERS applications [9]. The spatial arrangement and interparticle spacing of NPs on the substrate also influence hotspots formation, which is essential for achieving high signal amplification [10]. Extensive research has therefore focused on fabricating plasmon-active substrates by optimizing nanomaterial composition and structural properties. In line with this, theoretical simulations using the finite element method (FEM) have become essential for visualizing localized electromagnetic field distributions, which govern EF in SERS substrates. Incorporating theoretical analysis enables better understanding and prediction of experimental SERS outcomes.

Noble metal NPs, including gold (Au), silver (Ag), copper (Cu) and platinum (Pt), exhibit unique LSPR properties, making them ideal for SERS. Au and Ag NPs are favored due to their optimal LSPR frequencies and high sensitivity for analyte detection. Bimetallic Au-Ag NPs further enhance SERS performance by leveraging the properties of both metals [11]. Au provides chemical stability, while Ag offers enhanced plasmonic properties, reduced optical losses and a broader resonance range for higher EF. Studies have shown that Au-Ag NPs outperform their monometallic counterparts in sensitivity [12, 13]. Additionally, integrating reduced graphene oxide (rGO) as a hybrid substrate amplifies SERS performance. The two-dimensional (2D) planar structure of rGO provides a uniform surface for NP deposition and prevents agglomeration [14, 15]. The presence of functional groups such as hydroxyl (-OH), carboxyl (-COOH) and epoxy on rGO improves NPs binding through chemical and electrostatic interactions, as well as enhancing analyte adsorption and plasmonic coupling [16]. Researchers often use graphene and metal composite approach for SERS enhancement. For instance, Yu et al. [17] fabricated rGO-Au/Ag core-shell nanorods (NRs) via seed-mediated growth method, requiring multiple synthesis and purification steps. Similarly, Zhang et al. [18] developed graphene/Au NPs focusing on monometallic performance. However, these studies are limited in comparing monometallic and bimetallic NPs on rGO and often involve complex synthesis routes without incorporating theoretical validation. This highlights the need to analyze plasmonic interactions, optimize rGO concentration and evaluate the impact on EF for enhanced SERS performance.

In this study, we evaluate SERS efficiency of monometallic (Au or Ag) and bimetallic (Au-Ag) NPs embedded on rGO. Compared to previous bimetallic rGO-based SERS substrates, this work systematically compares mono- and bimetallic NPs and integrates experiments with FEM simulations to understand plasmonic enhancement. Near-field simulations of Au, Ag and Au–Ag NPs were conducted to predict near-field behavior and hotspot generation in between the NPs. The experimental work involves optimizing the formation of rGO thin-film to provide a conductive matrix for uniform NPs embedment and enhanced plasmonic interactions. The combination of Au and Ag aims to maximize Raman signal enhancement through optimized LSPR effects. To quantify this enhancement, the EF values were analyzed using rhodamine 6G (R6G) as a Raman reporter. This comparative evaluation highlights differences in plasmonic performance between monometallic and bimetallic NPs. Additionally, the effect of different R6G concentrations on SERS signal intensity was also investigated. These findings provide valuable insights into plasmonic enhancement mechanisms and contribute to the development of high-performance SERS platforms for molecular detection.

Theoretical Methods

SERS Enhancement

This section describes the theoretical basis for quantifying enhancement in SERS substrates. The EF in SERS measures the amplified Raman scattering when molecules adsorb near or on plasmon-active substrates [19]. The excitation of LSPRs in metal NPs is fundamental to the EM enhancement mechanism in SERS. LSPRs arise from the collective oscillation of conduction electrons in response to incident light (E_{inc}), generating intense localized EM fields near the NPs surfaces. When incident light (ω_L) excites electron oscillations in metallic nanostructures, a localized plasmon EM field (E_{loc}) stronger than the E_{inc} is induced. This enhanced local field intensifies Raman excitation, increasing scattering efficiency. The induced Raman dipole moment (μ) of a molecule is proportional to the E_{loc}, expressed as:

$$\mu = \alpha E_{loc}, \tag{1}$$

where α is the Raman polarizability [20]. The local field EF at the incident light frequency, ($M_{\mathrm{loc}}(\omega_{\mathrm{L}})$) is given as:

$$M_{loc}(\omega_L) = \left(\frac{|E_{loc}(\omega_L)|}{|E_{inc}(\omega_L)|}\right)^2. \tag{2}$$

Similarly, the scattered Raman light (ω_{R}) undergoes field enhancement. Due to optical reciprocity, this is approximated as $M_{\mathrm{rad}}(\omega_{\mathrm{R}}) \approx M_{\mathrm{loc}}(\omega_{\mathrm{L}})$, where $M_{\mathrm{rad}}(\omega_{\mathrm{R}})$ is the field enhancement at the Raman scattered frequency. Thus, the EM EF combines both excitation and emission enhancements [20]. Assuming ($\omega_{\mathrm{R}} \approx \omega_{\mathrm{L}}$), it simplifies to:

$$M_{loc}(\omega_L) M_{rad}(\omega_R) \approx \left(\frac{|E_{loc}(\omega_L)|}{|E_{inc}(\omega_L)|}\right)^2 \times \left(\frac{|E_{loc}(\omega_L)|}{|E_{inc}(\omega_L)|}\right)^2 \approx \left(\frac{|E_{loc}(\omega_L)|}{|E_{inc}(\omega_L)|}\right)^4. \tag{3}$$

This $|E|^4$ dependence in the hotspots is a key to Raman enhancement in SERS. The efficiency of this enhancement is governed by LSPR, which depends on the dielectric properties of the metal (ε_{m}) and surrounding medium (ε_{d}) [21]. The resonance condition is given by:

$$Re(\varepsilon_m + 2\varepsilon_d) = 0. \tag{4}$$

Achieving strong plasmonic resonance maximizes local field enhancement and hotspots intensity. However, plasmonic tuning in monometallic NPs is limited by intrinsic dielectric properties. While, the synergy between Au and Ag enhances LSPR and hotspot intensity. This can be described by the field EF in bimetallic NPs:

$$EF_{bimetallic} \propto |M_{loc,Au}(\omega) + M_{loc,Ag}(\omega)|^4, \tag{5}$$

where $M_{\mathrm{loc,\,Au}}(\omega)$ and $M_{\mathrm{loc,\,Ag}}(\omega)$ are the field contributions from Au and Ag, respectively. Quantitative studies have shown that the hybrid dielectric properties of bimetallic NPs optimize LSPR condition [22].

Near-Field Simulation

This section presents finite element simulations to predict near-field behavior and hotspot generation in Au–Ag NPs. Prior to the experimental work, near-field enhancement and surface plasmon resonance (SPR) in metallic NPs were analyzed using the FEM. The simulation model consisted of four NPs with 5 nm radius and 2 nm interparticle gaps to study hotspot generation at nanoscale distances. The NPs were modeled in a mixed air and rGO dielectric environment to represent the wrinkled morphology of thin-film. The 2D model is governed by Maxwell's equations [23], with the time-harmonic wave equation for the electric field (E) expressed as:

$$\nabla \times \left(\frac{1}{\mu_r}(\nabla \times E)\right) - k_0^2\left(\epsilon_r - \frac{j\sigma}{\omega\varepsilon_0}\right)E = 0. \tag{6}$$

Here, $k_0 = \omega c^{-1}$ is the wavenumber, ω is the angular frequency and $c = (\varepsilon_0\mu_0)^{1/2}$ is the speed of light in vacuum. ε_0 and μ_0 are the free space permittivity and permeability while ε_r and μ_r represents the relative permittivity and permeability of the metal, respectively. The solution of Eq. (6) was obtained using FEM, which involves dividing the simulation domain into smaller subdomains forming a mesh. Figure 1 (a) shows the mesh of the simulation with 2556 triangular elements, 38 vertex elements and 0.03839 minimum element quality. The dielectric response of the metal NPs was modelled using the Drude equation:

$$\varepsilon(\omega) = \varepsilon_\infty - \frac{\omega_p^2}{\omega^2 + i\gamma\omega} \tag{7}$$

where ε_∞ is the high-frequency dielectric constant, ω_p is the plasma frequency and γ is the damping constant. For bimetallic NPs, the model includes interband transitions, enhancing LSPR by broadening the resonance range and reducing optical losses.

Figure 1 (b) shows the simulated electric field intensity ($|E|^2$) distribution at the hotspots of Au-Ag NPs at 535 nm excitation wavelength. The $|E|^2$ profile extracted along a diagonal cut through the hotspots of different NPs is shown in Fig. 1 (c). The sharp peaks corresponded to the maximum $|E|^2$, where the highest intensity was obtained for Au-Ag NPs at 8.56×10^5, surpassing the values for Au and Ag monometallic NPs at 6.96×10^5 and 6.97×10^5, respectively. This was due to the hybrid dielectric properties that optimize LSPR for Au-Ag NPs. Figure 1 (d) further shows the $|E|^2$ decay trend with increasing interparticle distances. The maximum $|E|^2$ was obtained at closest simulated distance (2 nm) and this value was gradually decreased with increasing distance. This highlights the role of nanoscale interparticle spacing in optimizing hotspot intensity and SERS performance. According to Mie theory, NP size governs LSPR by modulating absorption and scattering cross-sections, which directly affect EM field intensity [24, 25]. Since the SERS EF scales with the fourth power of the local field, even small variations in near-field strength can result large changes in enhancement. The FEM model, however, is based on an idealized arrangement of spherical NPs on a

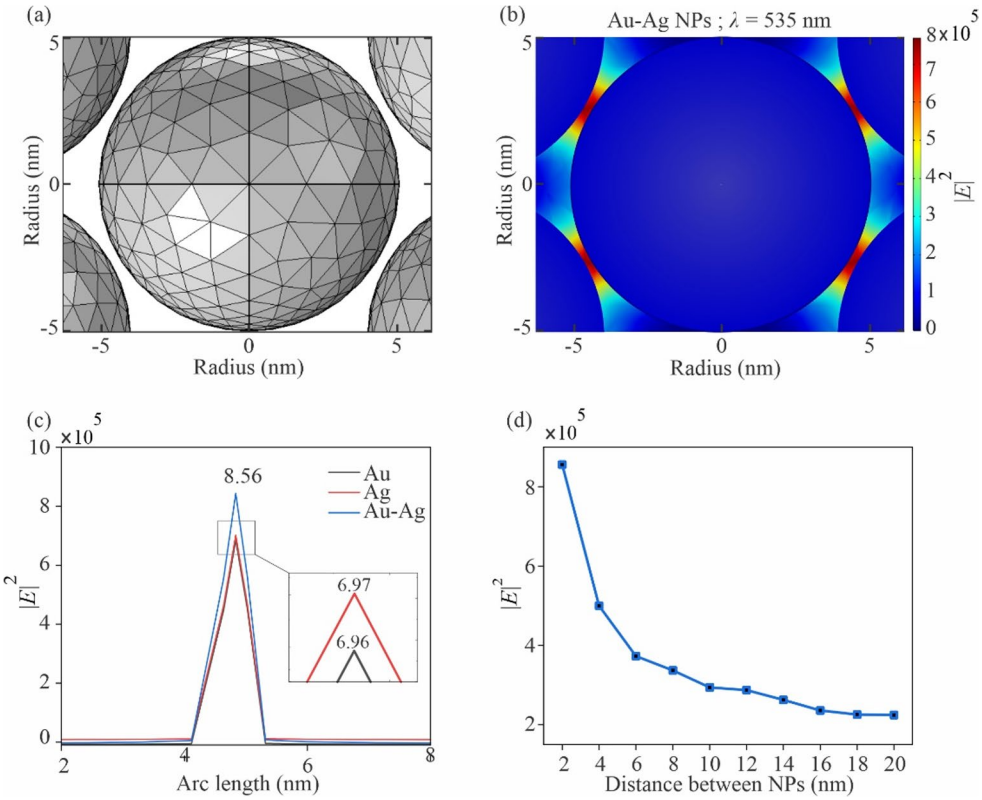

Fig. 1 (**a**) FEM mesh of the model. (**b**) Simulated $|E|^2$ distribution at the hotspots of Au-Ag NPs. (**c**) $|E|^2$ along the diagonal arc in the NPs gap, with an inset for Au and Ag NPs. (**d**) $|E|^2$ at varying interparticle distances for Au-Ag NPs

flat dielectric surface, which does not capture the wrinkled rGO morphology observed experimentally. Therefore, the simulations provide qualitative insight into plasmonic coupling and field enhancement trends rather than quantitative predictions. For comparison, FEM simulations performed in air without the rGO dielectric background are provided in Fig. S1.

Experimental Works

1 Chemicals

Gold (III) chloride trihydrate ($HAuCl_4 \cdot 3H_2O$, ≥99.9%, Cat. No. 938122), graphite powder (Cat. No. 282863), hydrochloric acid (HCl, Cat. No. 109060), Rhodamine 6G (R6G, 95.0%, Cat. No. 252433) and sodium borohydride ($NaBH_4$, >98%, Cat. No. 452882) were purchased from Sigma-Aldrich. Silver nitrate ($AgNO_3$, Cat. No. AR1246) was obtained from RCI Labscan Limited. Trisodium citrate ($Na_3C_6H_5O_7$, Cat. No. 106448), sodium nitrate ($NaNO_3$, ≥99.5%, Cat. No. V800390), potassium permanganate ($KMnO_4$, Cat. No. 105082), sulfuric acid (H_2SO_4, 98.0%, Cat. No. 11208) and hydrogen peroxide (H_2O_2, 30.0%, Cat. No. 107209) were purchased from Merck. All chemicals were used as received without further purification.

2 Synthesis of NPs

The NPs were synthesized via a bottom-up technique. The Au NPs were synthesized using $HAuCl_4.3H_2O$ as the metal precursor, TSC and $NaBH_4$ [26]. A solution of 0.9 mL $HAuCl_4$ trihydrate (0.01 M) was heated in distilled water. Then, 0.5 mL TSC (0.01 M) and 0.12 mL $NaBH_4$ (0.1 M) were added, turning the solution into dark purple, to signify Au NPs formation. The solution was stirred for 15 min, then centrifuged at 4000 rpm for purification. The Ag NPs were synthesized by mixing 10 mL PVA (0.3%) and 10 mL $AgNO_3$ (0.01 M) in an ice bath. 10 mL $NaBH_4$ (0.002 M) was added dropwise under stirring. The resulting solution formed a yellowish-dark brown, signifying the formation of Ag NPs [27]. After 15 min of stirring, the solution underwent centrifugation for separation. Bimetallic Au-Ag NPs were fabricated by boiling 39 mL of distilled water at 100 °C with stirring. Then, 0.5 mL of $HAuCl_4$ (0.01 M) and 1.5 mL of $AgNO_3$ (0.01 M) were added, followed by 4 mL of TSC (0.1 M) solution. After stirring for 15 min, the solution was cooled and stored at room temperature [28].

3 Synthesis of rGO

Graphene oxide (GO) was fabricated from natural graphite powder using a modified Hummer's method [29]. Briefly, graphite, $NaNO_3$ and H_2SO_4 were mixed and stirred below 5 °C using an ice bath. Under vigorous stirring, $KMnO_4$ was added and stirred for two hours. Then, the mixture was allowed to cool to room temperature, then heated to 35 °C for 30 min. 125 mL of distilled water was added to dilute the solution and then heated to 70 °C. The mixture was poured into 500 mL distilled water to precipitate for 12 h. H_2O_2 was added to remove the unreacted $KMnO_4$. The mixture was precipitated, purified through centrifugation and redispersion to achieve neutral pH. The resulting GO slurry was dried in a vacuum oven for 48 h before being grounded into powder. Subsequently, the GO underwent a thermal reduction process to form rGO in a furnace oven at 300 °C for 1 h, with a heating rate of 5 °C per minute.

4 Preparation of rGO thin-film and SERS substrates

Silicon (Si) chips were used as the solid base for the SERS substrates and underwent surface optimization via a double hydroxylation process to enrich -OH groups, enhancing surface hydrophilicity for improved substrate bonding. Initially, the substrates were immersed in a piranha solution (H_2SO_2:H_2O_2 = 1:1) at room temperature for 20 min. Then, they were submerged in a hydroxylation solution (distilled water: HCl: H_2O_2 = 6:1:1) for 20 min at 85 °C, introducing -OH functional groups onto the Si surface. For rGO thin-film fabrication, 1 mg, 2 mg and 4 mg of GO were dispersed in 1 mL distilled water, sonicated at 80 °C and spin-coated onto hydroxylated Si substrates. The coated substrates were annealed at 300 °C for one hour to obtain rGO thin-films. The SERS substrates were then prepared by dispersing 2 mg of GO into 1.5 ml of Au, Ag and Au-Ag NP solutions. The mixtures were sonicated at 80 °C and spin-coated onto hydroxylated Si substrates. Finally, the coated substrates were annealed at 300 °C for one hour at a heating rate of 5 °C/minutes to improve NPs adhesion, forming Au/rGO, Ag/rGO and Au-Ag/rGO substrates.

5 Characterizations

The synthesized substrates were characterized for optical and structural properties. Ultraviolet-visible (UV-Vis) spectroscopy analyzed the plasmonic behavior of NPs using a Shidmazu UV-1800 spectrophotometer model. Particle size analysis (PSA) was performed using Malvern Zetasizer Nano ZSP to determine the size distribution of the NPs, ensuring sample uniformity. The morphology and surface characteristics of the materials were observed using a Hitachi SU8020 field emission scanning electron microscope (FESEM) and Jeol JEM-ARM 200 F high resolution transmission electron microscopy (HRTEM). These imaging techniques provided detailed insights into the NPs' morphology. X-ray diffraction (XRD) analysis was used to determine the crystalline structure of GO and rGO using a Rigaku XtaLAB P200 diffractometer. Fourier transform infrared (FTIR) spectroscopy was performed using a Thermo Nicolet iS10 spectrometer to identify and confirm the functional groups present in GO and rGO before and after reduction. This multi-technique approach validated the synthesized materials for SERS analysis.

6 Raman measurements

The Raman spectra of rGO thin-films (1 mg, 2 mg and 4 mg) and SERS substrates (Au/rGO, Ag/rGO and Au-Ag/rGO) were recorded using a UniDRON confocal microscopy Raman spectrometer equipped with 532 nm and 785 nm excitation lasers. The laser power was set at 20% to optimize signal detection without causing damage. Before measurements, the instrument was calibrated with a single crystal Si reference for accuracy. The collected spectral data were processed using OriginPro 2022 (OriginLab), smoothed at 50 cm^{-1} to reduce noise and corrected for baseline interference. Prominent peaks were labelled and analyzed to extract structural and compositional information of the material. This step was critical for assessing the performance of the fabricated SERS substrates.

7 EF testing using R6G

SERS performance of the substrates was evaluated using R6G as a Raman reporter. Aqueous R6G solutions with varying concentrations ranging from 10^{-2} M to 10^{-10} M were prepared. For each concentration, 2 µL of the solution was dropped onto the Au-Ag SERS substrates and allowed to dry under ambient conditions. To calculate the SERS EF, a 10^{-1} M R6G solution (2 µL) was also deposited onto a bare Si chip and dried for Raman spectral analysis. Raman spectra were recorded at three random spots on each substrate to assess spot-to-spot reproducibility. EF was calculated using the following formula:

$$\mathrm{EF} = \frac{I_{\mathrm{SERS}}}{I_{\mathrm{Bare}}} \times \frac{C_{\mathrm{Bare}}}{C_{\mathrm{SERS}}}, \tag{8}$$

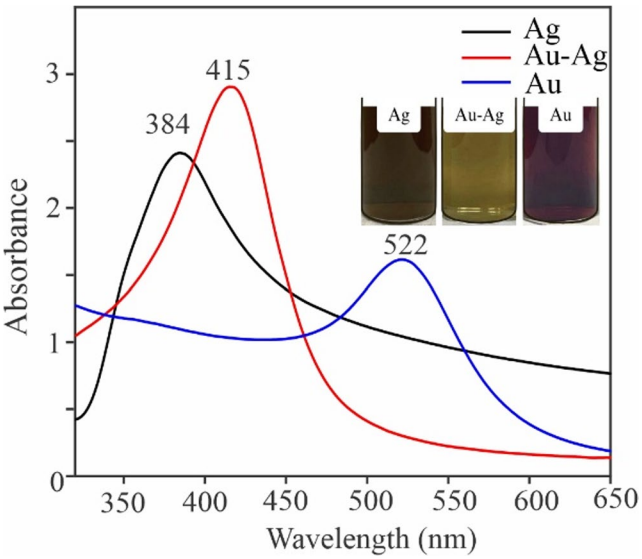

Fig. 2 The absorption spectra of Au, Ag and Au-Ag NPs, with an inset of NPs solution colors

where I_{SERS} and I_{Bare} are the Raman intensities from SERS substrate and bare substrate, respectively. C_{SERS} and C_{Bare} are the corresponding R6G concentrations.

Results and Discussion

Properties of NPs

Optical Properties

Figure 2 shows the absorption spectra measured using a UV–Vis spectrometer. The spectra revealed differences in wavelength and absorption intensity, indicating variations between Au, Ag and Au-Ag NPs. Absorption maxima for Ag and Au NPs were observed at 384 nm and 522 nm, respectively. Conversely, bimetallic Au-Ag NPs exhibited a single peak at 415 nm indicating a homogeneous alloy structure [30]. This homogeneity confirmed that the bimetallic NPs are an alloy rather than a core-shell structure, where multiple peaks would have been expected. The alloying effect broadened the plasmon resonance, minimized optical losses and enhanced resonance intensity due to the synergistic interaction between Au and Ag. The bimetallic Au-Ag NPs displayed higher absorption intensity than the monometallic NPs, indicating stronger plasmonic activity [31]. This enhancement is further amplified by the dominant amount of Ag, which enhanced their EM field properties and plasmonic effectiveness. These properties make them highly effective for applications needing strong plasmonic activity.

The inset in Fig. 2 shows the macroscopic view of different colors for the synthesized Au, Ag and Au-Ag NPs solutions. It revealed distinct colorations in their respective NPs solutions, providing a visual cue to their unique optical properties. The Au NPs resulted in a dark purple colour solution, while Ag NPs solution appeared in dark brown colour. In the case of the bimetallic Au-Ag NPs, the solution was in yellow colour. This was due to a higher concentration of Ag compared to Au with the ratio of 1:3. Thus, the colour of Ag NPs played a more significant role in this sample. Colour variations of metal NPs were attributed from the unique optical properties and SPR effect of the constituent metals [32]. SPR occurs when conduction electrons resonated with incident light at specific wavelengths. The arrangement and interaction of Au and Ag atoms in the NPs further influenced their collective electron oscillations, known as plasmons [33]. Ultimately, the plasmon resonances determine the absorption and scattering properties of NPs, which in turn influenced their visual colour appearance.

Table 1 Wavelength, average size and zeta potential for Au, ag and Au-Ag NPs

Sample	Wavelength (nm)	Average Size (nm)	Average Zeta Potential (mV)
Au	522	29.60	−40.5
Ag	384	33.35	−25.2
Au-Ag	415	72.60	−33.1

Morphology and Structural Analysis

The particle size and zeta potential of the NPs were analyzed using PSA, as summarized in Table 1. Average sizes were 29.60 nm, 33.35 nm and 72.60 nm for Au, Ag and Au-Ag, respectively. Negative zeta potential values confirmed colloidal stability due to electrostatic repulsion by anionic borohydride species. HRTEM analysis provided more precise structural and morphological insights, confirming NP sizes ranging from 10 to 65 nm. The size discrepancies compared to PSA measurements were due to PSA measuring the hydrodynamic diameter in solution, whereas HRTEM captured the core size in a dried state. Figure 3 (a-c) show that the NPs were spherical in shape. Lattice fringes with interplanar spacings of 0.20 nm, representing the (200) plane of face-centered cubic (FCC) Ag [34] and 0.23 nm, indicating the (111) plane of FCC Au [35], were observed. These features indicate the high crystallinity of the synthesized NPs, which was crucial for plasmonic interaction and SERS performance. Selected area electron diffraction (SAED) patterns in Fig. 3 (d-f) show SAED patterns indicating growth along (111), (200), (220) and (311) planes. For comparison, Table 2 presents the lattice spacing (d_{hkl}) values for the (111) plane, including standard reference values extracted from crystallographic information files (CIFs) available in crystallographic

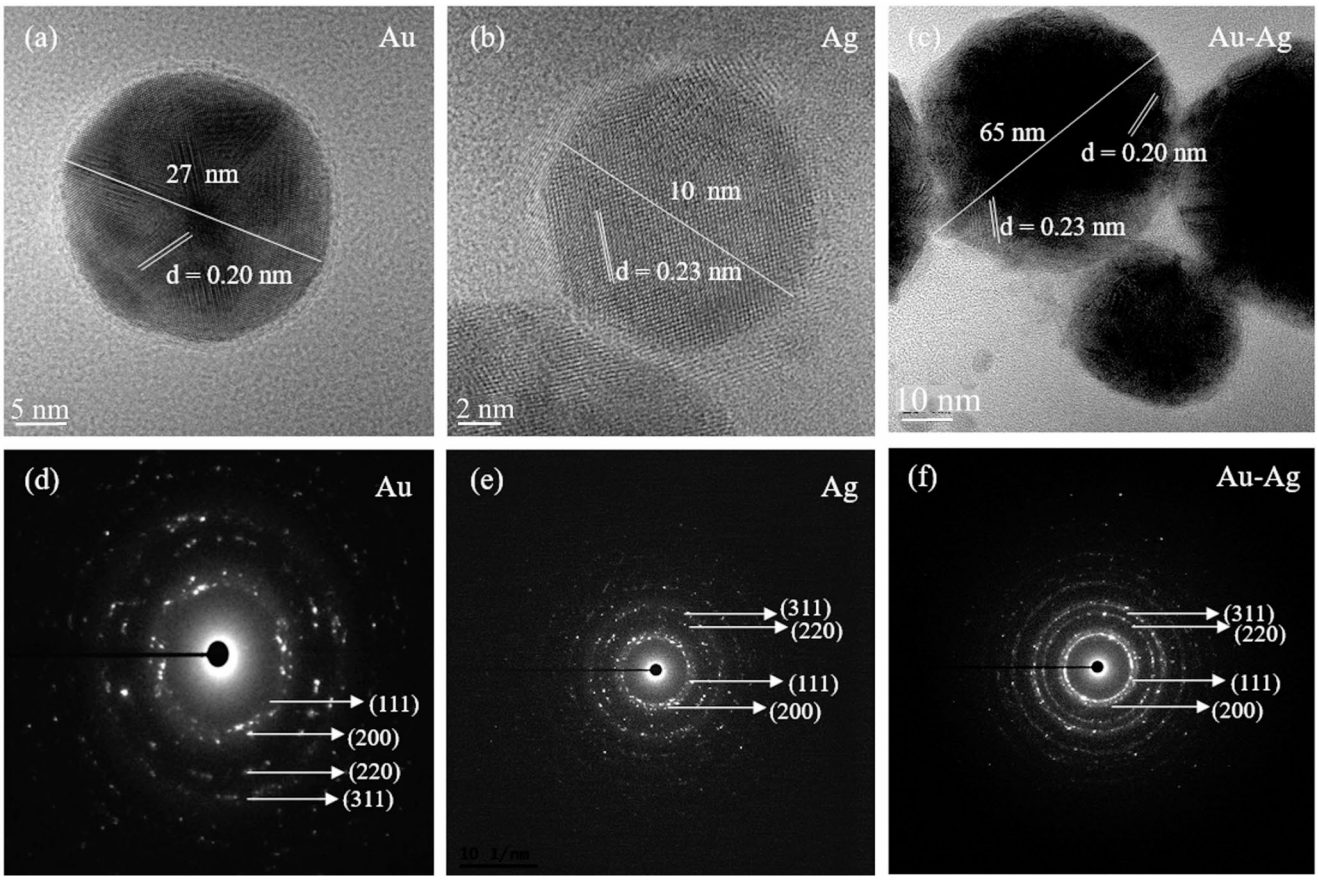

Fig. 3 (**a**-**c**) HRTEM images of Au-Ag, Au and Ag NPs with interplanar spacing, (**d**-**f**) SAED pattern of Au-Ag, Au and Ag NPs

Table 2 Reported and experimental d_{111} values for Au, ag and Au-Ag NPs

Sample	CIF Reference (Å)	Experimental (Å)	Other studies (Å)	Ref.
Au	2.35	2.36	2.36	[36]
Ag	2.40	2.39	2.36	[34]

databases, the experimental values from this study and values from previous studies. The d_{111} value of Au-Ag NPs (2.38 Å), lies between the experimental values for Au and Ag, confirming alloy formation.

To gain deeper insights and validate the formation of bimetallic Au-Ag NPs, high-angle annular dark-field scanning transmission electron microscopy (HAADF-STEM) and energy-dispersive X-ray spectroscopy (EDX) were performed. These advanced techniques provided detailed compositional and structural information at the nanoscale. This was crucial for understanding the distribution and interaction of different metal components within the NPs. Figure 4

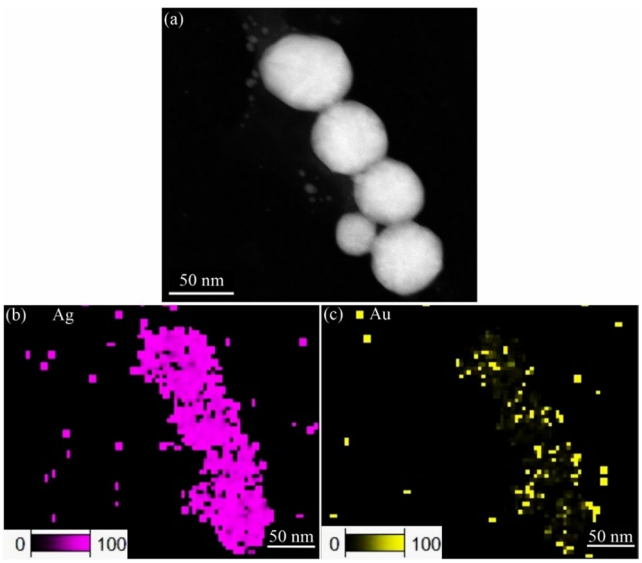

Fig. 4 (**a**) HAADF-STEM image, (**b**-**c**) EDX elemental mapping illustrating Au-Ag intermix (scale bar: 50 nm)

(a) shows the HAADF image of bimetallic NPs, demonstrating a contrast between Au and Ag components. In HAADF-STEM mode, the intensity correlates with atomic number of the elements, where brighter regions indicate Ag (lighter element) and darker regions correspond to Au (heavier element) [37]. The image vividly illustrates the intertwined distribution of Ag and Au elements within the bimetallic NPs. Figure 4 (b-c) show the presence of Ag signals (pink) and Au signals (yellow), which serve as a crucial marker for the formation of bimetallic NPs with an alloy structure. The lower intensity of the Au signal is attributed to the 1:3 molar ratio of Au to Ag used during synthesis, resulting in a higher Ag content in the NPs.

Properties of rGO

Raman Characterization

Figure 5 (a) shows the Raman spectrum of rGO, recorded using a 532 nm laser, showing D- and G-peaks and 2D band at 1345 cm^{-1}, 1580 cm^{-1} and 2695 cm^{-1}, respectively. The D-band represents disordered carbon atoms, while the G-band corresponds to C = C stretching vibrations in sp^2 carbon rings [38]. The 2D band is used to determine number of graphene layers [39]. The broad and weak intensity of 2D band indicates the presence of multilayer rGO sheets rather than single-layer graphene, consistent with previous reports [40]. Optimizing rGO concentrationis crucial for balancing its structural integrity and functional properties as a SERS substrate. A reduction in D- and G-band intensities were observed at 2 mg and 4 mg concentrations. This reduction occurred due to the inverse relationship between band intensity and the number of active scattering centers [41]. The 4 mg rGO sample formed a thicker layer, which can limit EM field penetration into the analyte layer and reduce available adsorption sites by blocking NP surfaces. Conversely, 1 mg rGO produced higher SERS intensity but was thin and non-uniform, resulting in poor surface adhesion and uneven NP distribution. The 2 mg rGO film provided a balance between surface coverage, hotspot formation and analyte accessibility, ensuring effective plasmonic enhancement. Film thickness influences the microstructure and EM properties of rGO coatings, affecting their overall performance [42].

The reproducibility of SERS signals was evaluated using the relative standard deviation (RSD) of D-peak intensities from three spots, as shown in Fig. 5 (b). The 2 mg rGO film exhibited the lowest RSD of 5.57%, indicating signal consistency compared to 1 mg and 4 mg rGO films with RSD values of 30.28% and 26.74%, respectively. This suggests that the optimized 2 mg concentration ensures high reproducibility, which is critical for practical SERS applications.

Furthermore, the D-to-G intensity ratios ($\frac{I_D}{I_G}$) were 0.92, 0.99 and 0.96 for 1 mg, 2 mg and 4 mg rGO concentrations, respectively. These values aligned with Shih et al. [43], where similar ratios were observed in rGO nanocomposites, indicating comparable defect densities in rGO materials. The higher defect density ratio for 2 mg rGO film indicates an optimal balance between defect sites and structural integrity, critical for analyte adsorption. Although single-layer graphene has enhanced properties, it is complex to produce. In contrast, few-layered graphene provides a practical balance offering high surface area for effective SERS substrate performance. An inset in Fig. 5 (a) shows the synthesized rGO powder.

Morphology and Structural Analysis

The surface morphology of rGO thin-film was examined using FESEM. As shown in Fig. 6 (a-c) the rGO appeared as a sheet-like structure with wrinkled and overlapping layers [44]. The inter-sheet gaps ranged from 35 to 856 nm, providing high surface area for analyte adsorption. This morphology provided an advantage for sensing applications, as the sheet-like appearance offered a large surface area that enhanced the interaction between the substrate and analytes, thereby improving

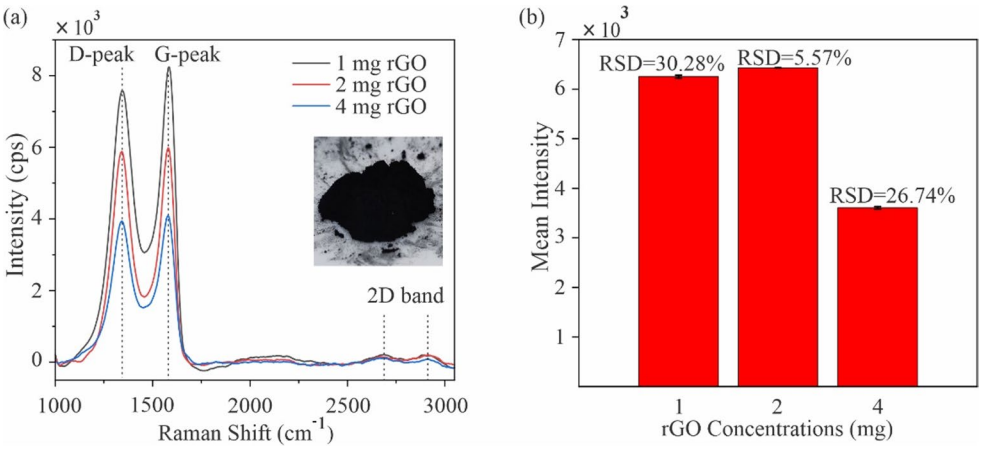

Fig. 5 (**a**) The Raman spectrum of rGO substrate at different concentrations, with inset of rGO powder. (**b**) Mean D-peak intensities with corresponding RSD values for rGO concentrations

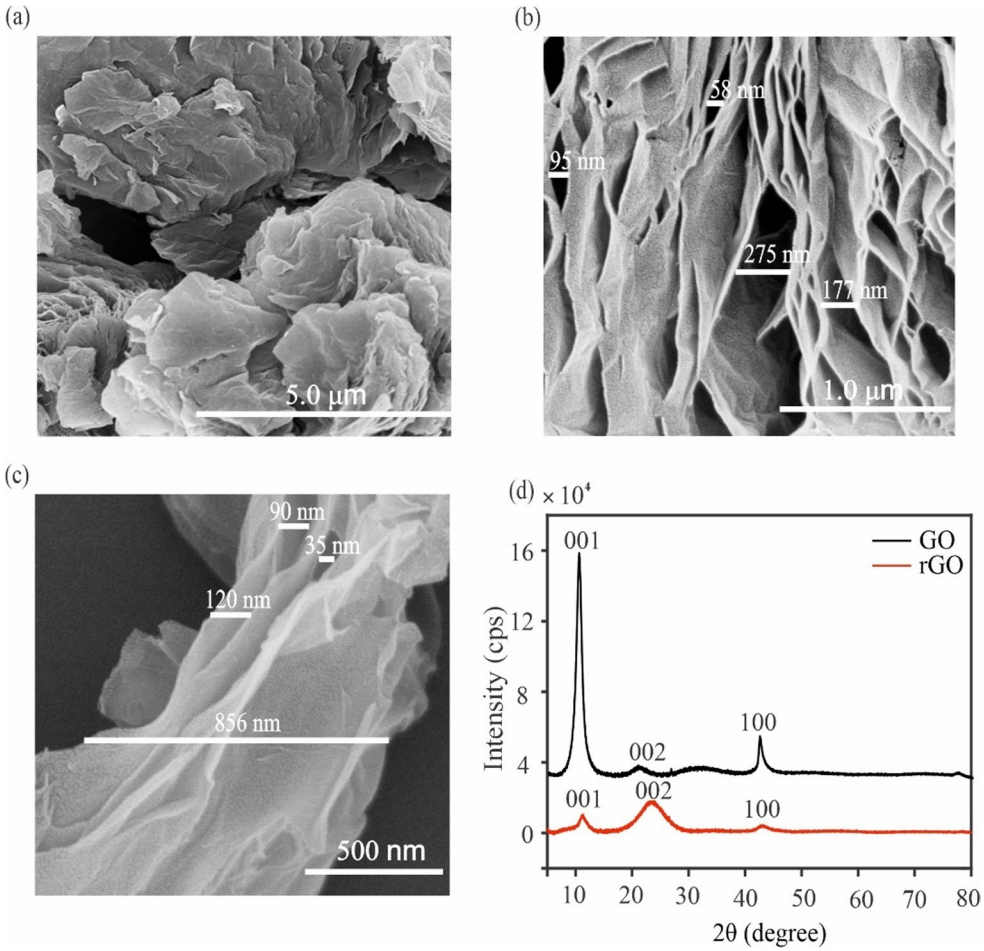

Fig. 6 FESEM image of the rGO thin-film at scale bar of (**a**) 5.00 µm, (**b**) 1.00 µm. and (**c**) 500 nm, with inter-sheet gaps of 35–856 nm (**d**) XRD patterns of GO and rGO indicating structural changes after reduction

detection sensitivity. Moreover, the overlapping and wrinkled layers provided numerous active sites that facilitated efficient analyte adsorption and detection [44]. These structural features were a result of partial restoration of sp^2 carbon networks during the reduction process. The retention of some oxygen functional groups further enhanced molecular interactions. The presence of defects and residual oxygen functional groups on the rGO sheets further contributed to improved molecular interactions [45]. This combination of high surface area, active site availability and enhanced molecular interactions validates rGO's suitability as a SERS substrate.

Figure 6 (d) shows the XRD patterns of GO and rGO, providing insights into the structural transformation of GO after the reduction process. The XRD analysis was conducted over a 2θ range from 5° to 80°. The GO diffraction pattern exhibited two prominent peaks at 2θ values of 10.36° and 42.33°, corresponding to the (001) and (100) planes, respectively. These diffraction peaks indicated the presence of oxygen-containing functional groups (-OH and -COOH) in the GO structure [46]. The observed peaks are characteristic of GO's layered structure, where intercalated oxygen groups expand the interlayer spacing. Additionally, a weak peak at 20.86°, corresponding to the (002) plane was observed. This feature likely arises from residual graphitic domains due to incomplete oxidation of graphite. Similar weak graphitic peaks have been reported in chemically synthesized GO prepared via modified Hummers' method [47, 48]. Upon reduction to rGO, significant changes were observed in the XRD pattern. The intensity of the (001) peak decreased significantly and the (100) peak nearly disappeared, indicating the removal of oxygen-containing groups. Conversely, the (002) peak became more prominent and shifted to 23.40°, reflecting a decrease in interlayer spacing due to the elimination of oxygen functionalities and partial restoration of sp^2 carbon lattice [14, 49]. These changes confirmed successful reduction of GO to rGO and its improved structural stability for SERS applications.

FTIR Characterization of GO and rGO

Figure 7 shows the FTIR spectra of GO and rGO, highlighting the changes in oxygen-containing functional groups after reduction. For GO, a broad absorption band at 3550 cm^{-1} corresponding to O-H stretching vibrations indicates the presence of hydroxyl groups. The peak at 1731.8 cm^{-1}

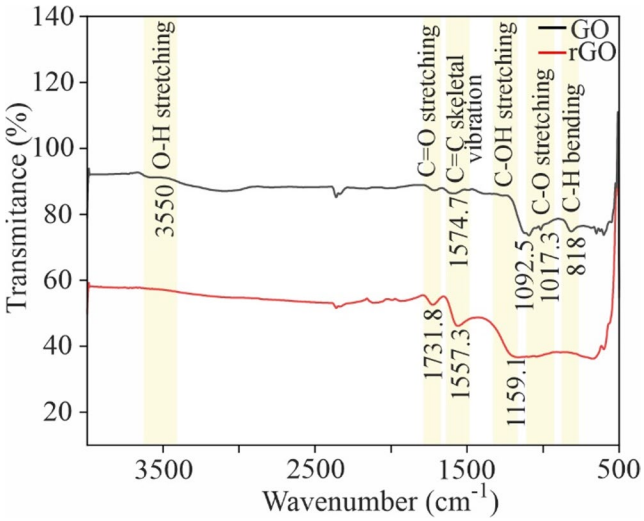

Fig. 7 FTIR spectra of GO and rGO

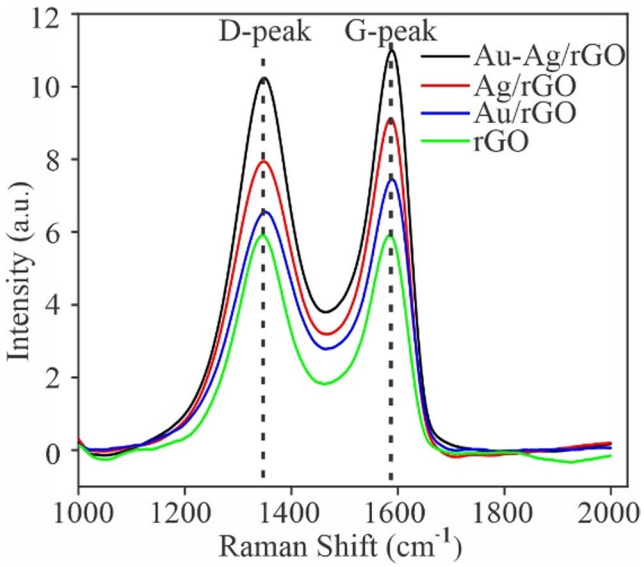

Figure 8 Raman spectra of rGO with and without metallic NPs

is attributed to C=O stretching of carboxyl groups, while the band at 1574.7 cm^{-1} arises from C=C skeletal vibrations of sp^2 carbon domains. Additional peaks at 1092.5 cm^{-1} and 1017.3 cm^{-1} for C–O stretching and the band at 818 cm^{-1} is due to C–H bending, confirming the abundance of oxygen functionalities in the GO structure [40, 50]. In contrast, the spectrum of rGO shows a reduction in the intensity of oxygen-containing peaks, while the C=C skeletal band shifts to 1557.3 cm^{-1} and becomes more prominent. These changes confirm the partial removal of oxygen functional groups and the partial restoration of sp^2 carbon networks during thermal reduction. This observation aligns with the XRD analysis, which showed the decrease of the 001 peak of GO and the more prominence of the 002 graphitic peak in rGO. The retention of a small fraction of oxygen-containing groups is advantageous, as they provide active anchoring sites for NP deposition and enhance binding interactions with the hydroxylated Si substrate.

Properties of SERS Substrates

Raman Analysis of Substrates

Figure 8 shows the Raman spectra of 2 mg rGO embedded with Au, Ag and Au-Ag NPs, recorded using a 532 nm laser, obtaining characteristic D- and G-peaks at 1345 cm^{-1} and 1580 cm^{-1}, respectively. Among the substrates, Au-Ag/rGO exhibited the highest peak intensities, demonstrating enhanced plasmonic activity compared to monometallic Au/rGO and Ag/rGO. This enhancement was attributed to the synergistic plasmonic effects between Au and Ag, which generated stronger localized EM fields at hotspots. The $\frac{I_D}{I_G}$ ratio decreased after NPs incorporation. The $\frac{I_D}{I_G}$ ratio values for Au/rGO, Ag/rGO and Au-Ag/rGO were 0.88, 0.87 and 0.93, respectively, compared to the higher value of 0.99 for pristine rGO. This decrease suggests a reduction in rGO defects, likely from charge transfer and stabilization effects, while maintaining its electronic properties. Furthermore, the $\frac{I_D}{I_G}$ ratio is directly related to improved SERS substrate performance, as it indicates an optimal balance between defect density and structural integrity. This balance ensures sufficient active sites for NPs anchoring and analyte adsorption, while maintaining the sp^2 carbon network necessary for strong plasmonic coupling and efficient Raman signal enhancement. These findings aligned with Yousefimehr et al. observing a decrease in $\frac{I_D}{I_G}$ for Au/rGO composites due to reduced rGO defects while retaining functionality [51]. Table 3 summarizes the $\frac{I_D}{I_G}$ values obtained for all substrates and compares them with literature values, indicating the improved SERS performance of the fabricated Au-Ag/rGO substrate.

Table 3 Comparison of $\frac{I_D}{I_G}$ ratios for Au/rGO, Ag/rGO and Au-Ag/rGO substrates with literature values

Sample	Spot 1	Spot 2	Spot 3	Average	Literature	Ref.
Au/rGO	0.84	0.91	0.88	0.88	0.81	[51]
Ag/rGO	0.84	0.90	0.87	0.87	0.78	[52]
Au-Ag/rGO	0.93	0.96	0.90	0.93	0.80	[53]

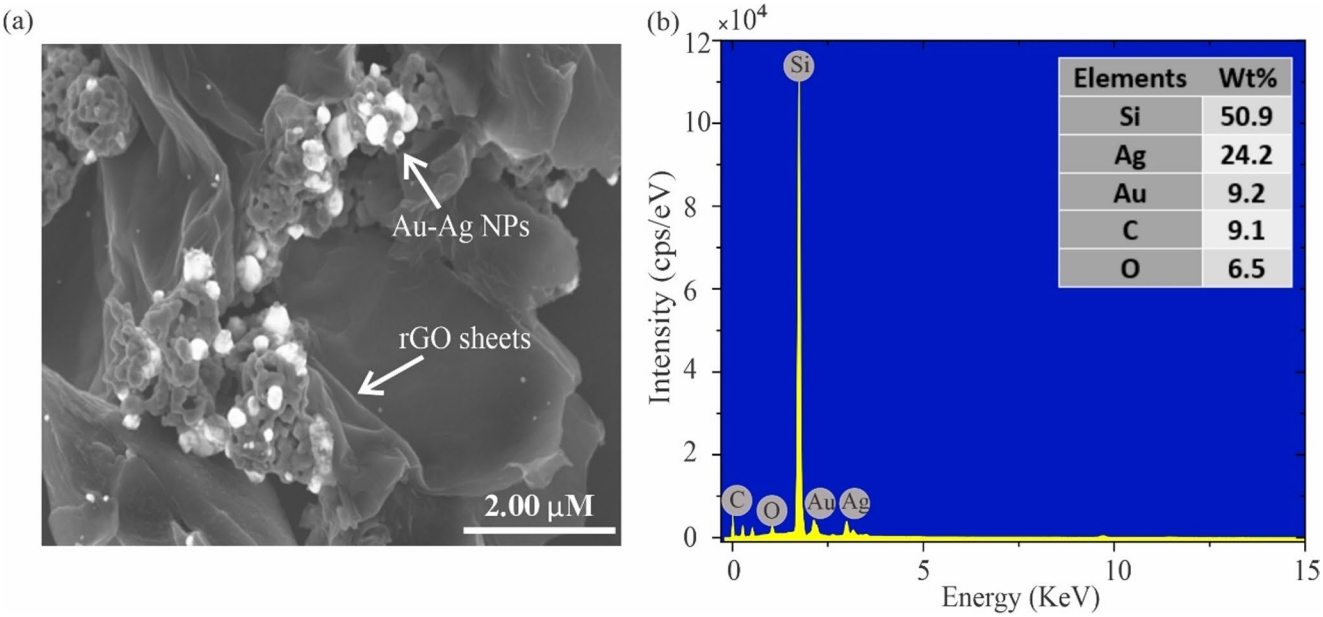

Fig. 9 (**a**) FESEM image and (**b**) EDX spectrum of Au-Ag/rGO SERS substrate on a Si chip

Surface Morphology of the SERS Substrate

Figure 9 (a) shows the FESEM image of the Au–Ag/rGO SERS substrate. The image reveals the sheet-like structure of rGO with bimetallic Au-Ag NPs distributed across its surface. The wrinkled and overlapping layers of rGO provided a large surface area and active sites for the attachment of Au-Ag NPs. The NPs appeared as bright, spherical clusters distributed across the rGO sheets with visible signs of uniformity and some degree of aggregation [54, 55]. The observed morphology indicated the successful attachment of the Au-Ag NPs onto the rGO surface. The combined morphology of Au-Ag/rGO SERS substrate were advantageous for sensing applications. The wrinkled rGO sheets provided a large surface area, while the spherical Au-Ag NPs created active sites for plasmonic interactions. This structural synergy enhanced analyte adsorption and promoted efficient electron transfer, improving the sensitivity and performance of the Au-Ag/rGO SERS substrate in detection systems.

The elemental composition of the substrate was determined using EDX analysis, as shown in Fig. 9 (b). The spectrum confirmed the presence of key elements, including Si (50.9 wt%), Ag (24.4 wt%), Au (9.2 wt%), carbon (9.1 wt%) and oxygen (6.5 wt%). The high percentage of Si was attributed to the use of a Si chip as the substrate during the EDX analysis. The significant presence of Ag compared to Au was consistent with the 1:3 bimetallic ratio used during synthesis, where a higher proportion of Ag was intentionally introduced. Ag contributed strongly to LSPR, which was essential for enhancing the plasmonic properties of the SERS substrate. The detected carbon and oxygen corresponded to the rGO matrix with the oxygen content likely resulting from residual oxygen-containing functional groups on rGO. These functional groups enhanced NPs attachment and improved the stability of the substrate. These results confirmed the successful incorporation of Au and Ag NPs onto the rGO structure, reflecting the controlled composition of the SERS substrate.

EF Evaluation of the SERS Substrate

Figure 10 (a) shows the Raman spectra of R6G adsorbed on Au/rGO, Ag/rGO and Au-Ag/rGO SERS substrates, recorded using a 532 nm green laser. The spectra displayed prominent bands at 613 cm^{-1}, 772 cm^{-1}, 1184 cm^{-1}, 1311 cm^{-1}, 1362 cm^{-1}, 1508 cm^{-1}, 1572 $cm^{-1}$and 1650 cm^{-1}. These bands correspond to specific vibrational modes of R6G molecules adsorbed on the substrate surface. For instance, the band at 1362 cm^{-1} corresponded to the C-C stretching mode of the aromatic ring. This highlighted the strong π-π interaction between R6G and the graphene-based substrates [56]. Similarly, other bands such as those at 613 cm^{-1} (C–C in-plane bending) and 772 cm^{-1} (C–H out-of-plane bending), reflected the skeletal and bending vibrations characteristic of R6G molecules. The identified vibrational modes confirmed the successful adsorption of R6G onto the SERS substrates. Consistent with prior studies, these findings confirmed the presence of R6G molecules on the substrate [17]. Table 4 provides a detailed summary of the observed Raman peaks and their vibrational assignments for R6G molecules on the SERS substrates.

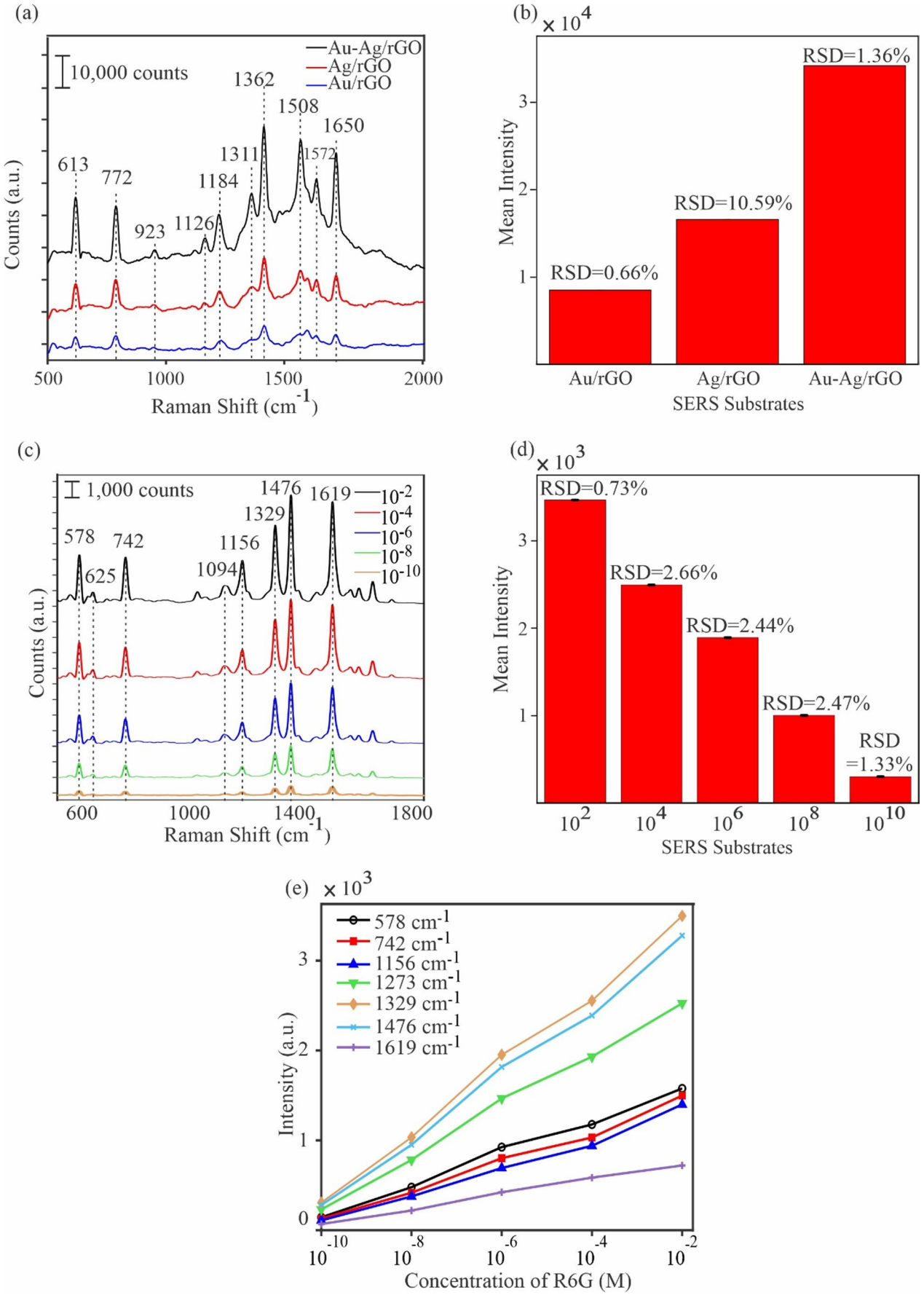
(a)
10,000 counts
Au-Ag/rGO
Ag/rGO
Au/rGO
613
772
923
1126
1184
1311
1362
1508
1572
1650
Counts (a.u.)
500
1000
1500
2000
Raman Shift (cm-1)
(b)
× 10^4
RSD=1.36%
RSD=10.59%
RSD=0.66%
Mean Intensity
Au/rGO
Ag/rGO
Au-Ag/rGO
SERS Substrates
(c)
1,000 counts
578
625
742
1094
1156
1329
1476
1619
10-2
10-4
10-6
10-8
10-10
Counts (a.u.)
600
1000
1400
1800
Raman Shift (cm-1)
(d)
× 10^3
RSD=0.73%
RSD=2.66%
RSD=2.44%
RSD=2.47%
RSD =1.33%
Mean Intensity
10^2
10^4
10^6
10^8
10^10
SERS Substrates
(e)
× 10^3
578 cm-1
742 cm-1
1156 cm-1
1273 cm-1
1329 cm-1
1476 cm-1
1619 cm-1
Intensity (a.u.)
10^-10
10^-8
10^-6
10^-4
10^-2
Concentration of R6G (M)

Fig. 10 Raman spectra of (**a**)Au-Ag/rGO, Ag/rGO and Au/rGO substrates at R6G concentration of 10^{-8}. (**b**) Mean Raman intensities with corresponding RSD values for Au/rGO, Ag/rGO and Au–Ag/rGO substrates. (**c**) R6G at varying concentrations. (**d**) Mean Raman intensities with corresponding RSD values for Au–Ag/rGO substrates at varying R6G concentrations. (**e**) Correlation of R6G intensity with concentrations

The EF was calculated via Eq. (8) to evaluate the enhancement capability of the SERS substrates. The EF values at different Raman shifts of R6G are summarized in Table 5. Among these, the 1362 cm^{-1} peak was selected due to its strongest intensity, ensuring reliable quantification for comparing substrate performance. The SERS EF values for Au/rGO, Ag/rGO and Au-Ag/rGO were 2.70 $\times 10^7$, 4.92 $\times 10^7$ and 1.12 $\times 10^8$, respectively. Notably, the EF of Au-Ag/rGO was approximately 2 times higher than Ag/rGO and 4 times higher than Au/rGO. This trend is consistent with FEM near-field simulations, which predicted stronger plasmonic coupling and higher hotspot intensity for Au–Ag NPs compared to their monometallic counterparts. This enhancement results from synergistic effects of plasmonic hotspots and improved charge transfer interactions facilitated by the bimetallic structure and rGO support. Such observations align with Yu et al. [17], who demonstrated that Au–Ag NRs on rGO exhibited significantly higher SERS enhancement than monometallic NPs, highlighting the role of rGO and its contribution to enhanced Raman intensities.

Table 6 compares these EF values with other studies. For instance, graphene/Au NPs (G/Au) [18], Ag/GO [57], core-shell gold-silver NPs (Au@Ag) [58] and Ag nanoflowers (NFs) with GO and Au NSs [59], have all reported significant SERS improvements. These findings support the conclusion that bimetallic structures, when integrated with rGO, can achieve exceptional SERS performance. In addition to EF performance, the practical aspects of the substrate, such as fabrication ease and cost-effectiveness, are crucial for real-world applications. Compared to other recent bimetallic systems, such as the G/Au film fabricated via chemical vapor deposition (CVD) [18], the present Au-Ag/rGO substrate offers a simpler and more scalable bottom-up fabrication route. Furthermore, unlike to magnetron sputtering approaches [58], this synthesis does not require expensive instrumentation or post-deposition annealing, thereby reducing operational costs. Compared to Ag@Au nanocavity-on-film substrates prepared via multistep seed-mediated growth, ligand-assisted epitaxial coating and prolonged self-assembly on Au films [58], our synthesis avoids complex synthetic control and multiple purification steps. In contrast to Ag NFs-GO-Au NS requiring sequential silanization, hierarchical Ag deposition, GO spin-coating and concentrated Au NSs coating [59], the current method eliminates lengthy substrate pretreatment and anisotropic particle synthesis steps. These advantages, coupled with the observed high EF values, demonstrate the strong potential of the fabricated substrate for cost-effective, scalable and reliable SERS sensing platforms. To analyze the reproducibility of the SERS substrate, the Raman intensity at 1362 cm^{-1} was measured at three random spots on the substrates, as shown in Fig. 9(b). The RSD values were 0.66%, 10.59% and 1.36% for Au/rGO, Ag/rGO and Au-Ag/rGO, respectively. These results demonstrate that the substrates exhibit good homogeneity and reproducibility.

Figure 10 (c-e) present the concentration-dependent SERS response of R6G on the Au-Ag/rGO substrate using a 785 nm laser. In Fig. 10 (c), the Raman spectra showed distinct peaks at 578 cm^{-1}, 742 cm^{-1}, 1156 cm^{-1}, 1273 cm^{-1}, 1329 cm^{-1}, 1476 cm^{-1} and 1619 cm^{-1}. These peaks correspond to the characteristic vibrational modes of R6G but differ in prominence and intensity compared to spectra obtained with a 532 nm laser. The use of the 785 nm laser reduces fluorescence interference, leading to clearer observation of certain vibrational modes. The intensity of these peaks increases linearly with higher concentrations of R6G, as shown in the plotted data. At higher concentrations, more R6G molecules are present within these enhanced regions, leading to stronger Raman signals [60]. The reproducibility of the substrate was further confirmed by calculating the RSD values at each concentration, which remained consistently low (0.73–2.66%) as shown in Fig. 10 (d). Moreover, Fig. 10 (e) also shows a linear increase in Raman intensity with R6G concentrations. It demonstrated the substrate's effectiveness in maintaining uniform enhancement across different concentrations, with detectable signals even at low concentrations (10^{-10} M). The low detection limit of 10^{-10} confirms the substrate's sensitivity toward trace-level analytes. At 532 nm, which overlaps with the Au (522 nm) and Au–Ag (415 nm) SPR bands, stronger plasmon coupling enhanced Raman intensity and yielded a higher EF. In contrast, 785 nm excitation, although off-resonance, minimized fluorescence background and enabled clearer detection of R6G peaks at trace concentrations [61]. The synergistic effects of the bimetallic system and graphene support in this study ensure enhancement, positioning Au-Ag/rGO as a promising SERS substrate for sensing applications.

Conclusion

In conclusion, this study successfully developed and evaluated SERS substrates based on monometallic (Au, Ag) and bimetallic (Au-Ag) NPs embedded on rGO. The optimized SERS substrates were fabricated by integrating spherical Au, Ag and Au-Ag NPs onto wrinkled rGO sheets, which provided a high surface area for NPs attachment. Raman measurements using R6G as a probe molecule confirmed

Table 4 Raman peaks and vibrational assignments for R6G molecule on SERS substrates

R6G Raman Shift (cm^{-1})	Assignment	Mode
613	C-C ring in-plane bending in xanthene/ phenyl rings	Skeletal bending
772	C-H out-of-plane bending	Bending
1184	C-H in-plane bending in xanthene ring	In-plane bending
1311	Hybrid mode (xanthene/phenyl rings and NHC_2H_5 groups	Hybrid vibrations
1362	Aromatic C-C stretching in xanthene ring	Stretching
1508	C-C stretching in xanthene ring	Stretching
1572	C-C stretching in phenyl ring	Stretching
1650	C-C stretching in xanthene ring	Stretching

Table 5 EF values of R6G at different Raman shifts on Au–Ag/rGO substrate

R6G Raman Shift (cm^{-1})	EF Value
613	5.35×10^7
772	4.64×10^7
1184	3.94×10^7
1311	5.64×10^7
1362	1.12×10^8
1508	1.01×10^8
1572	6.91×10^7
1650	9.06×10^7

Table 6 Comparative EF values for R6G of SERS substrates alongside literature values

Sample	EF value	Ref.
G/Au	1.40×10^5	[18]
Ag/GO	5.6×10^6	[57]
Ag@Au	2.0×10^7	[58]
Ag NFs-GO-Au NSs	2.59×10^7	[59]
Au-Ag NP/rGO	1.12×10^8	This study

that bimetallic Au-Ag/rGO exhibited the highest SERS enhancement. The EF of 1.12×10^8 for Au-Ag/rGO, compared to 2.70×10^7 for Au/rGO and 4.92×10^7 for Ag/rGO, validates the synergistic plasmonic interaction between Au and Ag. This interaction enhances localized EM fields and increases hotspots density, significantly amplifying the Raman signal. The FEM simulations supported these findings by correlating plasmonic behavior with experimental EF trends. The combined approach not only clarified the role of bimetallic synergy in enhancing hotspots intensity but also demonstrated a simpler and more scalable fabrication route compared to multi-step or instrument-intensive methods in prior studies. These findings highlight the effectiveness of bimetallic Au-Ag/rGO SERS substrates and their potential for practical applications in sensitive and accurate molecular detection. Future works will focus on evaluating the charge transfers between rGO and Au–Ag NPs via X-ray photoelectron spectroscopy (XPS) and ultraviolet photoelectron spectroscopy (UPS), quantifying thin-film thickness and uniformity via atomic force microscopy (AFM), as well as Raman stability tests to evaluate long-term substrate performance under real-world sensing conditions.

Supplementary Information The online version contains supplementary material available at https://doi.org/10.1007/s11468-025-03311-x.

Acknowledgements Authors wish to thank Universiti Teknologi Malaysia for supporting this work. This research was supported in full or in part with Kurita Asia Research Grant (23Pmy184) provided by Kurita Water and Environment Foundation.

Author Contributions All authors contributed to the study's conception and design. Nashmitta Pillai carried out the experimental work, data analysis and manuscript drafting. Liyana Shatar contributed with experimental support and data collection. Fatin H. Mustafa and Muhammad S.A. Aziz provided technical guidance and critical input. Ali A. Alwahib assisted with theoretical validation and analysis. Yasmin M. Kamil contributed to writing, review and editing. Fariza H. Suhailin supervised the project, analyzed data and reviewed the manuscript. All authors have read and approved the final manuscript.

Funding Open access funding provided by The Ministry of Higher Education Malaysia and Universiti Teknologi Malaysia. This research was supported in full or in part with Kurita Asia Research Grant (23Pmy184) provided by Kurita Water and Environment Foundation.

Data Availability The datasets generated during and/or analyzed during the current study are available from the corresponding author on reasonable request.

Declarations

Competing Interests Authors wish to thank Universiti Teknologi Malaysia for supporting this work. This research was supported in full or in part with Kurita Asia Research Grant (23Pmy184) provided by Kurita Water and Environment Foundation.

References

1. Li Z, Han X, Fu L, Shi G, Xu S, Wang M, Yuan W, Zhou W, Cui J (2024) Machine learning-driven Ag/SiO_2/Cu/rice leaf SERS platform for intelligent identification of pharmacodynamic substances. Microchem J 200:110459. https://doi.org/10.1016/j.microc.2024.110459
2. Yuan W, Han X, Shi G, Wang M, Zhou W, Cui J, Liu F, Li Z, Wu Y, Wang L (2024) Machine learning-driven multi-level composite SERS platform for trace detection of chlorogenic acid as pharmacodynamic substance in honeysuckle. Optics Laser Technol 169:109911. https://doi.org/10.1016/j.optlastec.2023.109911
3. Li Ming, Cushing SK, Zhou G, Wu N (2020) Molecular hot spots in surface-enhanced Raman scattering. Nanoscale 12:22036–22041. https://doi.org/10.1039/d0nr06579j
4. Cong S, Liu X, Jiang Y, Zhang W, Zhao Z (2020) Surface enhanced Raman scattering revealed by interfacial charge-transfer transitions. Innovation 1:100051. https://doi.org/10.1016/j.xinn.2020.100051
5. Zhou Z, Bai X, Li P, Wang C, Guo M, Zhang Y, Ding P, Chen S, Wu Y, Wang Q (2021) Silver nanocubes monolayers as a SERS substrate for quantitative analysis. Chinese Chem Lett 32:1497–1501. https://doi.org/10.1016/j.cclet.2020.10.021
6. López-Lorente ÁI (2021) Recent developments on gold nanostructures for surface enhanced Raman spectroscopy: Particle shape, substrates and analytical applications. A review. Anal Chim Acta 1168:338474. https://doi.org/10.1016/j.aca.2021.338474
7. Parambath JBM, Kim G, Han C, Mohamed AA (2022) SERS performance of cubic-shaped gold nanoparticles for environmental monitoring. Res Chem Intermediates 49:1259–1271. https://doi.org/10.1007/s11164-022-04913-4
8. Cheng H, Wang K, Gao R, Fu SY, Wang XT, Lin JS, Liu Y, Sun X, Yang Z, Duan X, Zhang YJ, Hu J, Liu JF (2024) Monodisperse, highly spherical, single crystalline Au nanospheres for uniform and reproducible hot spots in surface-enhanced Raman scattering at the single-particle level. Nano Letters 24:16374–16382. https://doi.org/10.1021/acs.nanolett.4c04951
9. Dey P (2023) Aiming for maximized and reproducible enhancements in the obstacle race of SERS. ACS Meas Sci Au 3:434–443. https://doi.org/10.1021/acsmeasuresciau.3c00037
10. Sahu AK, Raj S (2022) Effect of plasmonic coupling in different assembly of gold nanorods studied by FDTD. Gold Bull 55:19–29. https://doi.org/10.1007/s13404-022-00307-x
11. Manchala S, Nagappagari LR, Venkatakrishnan SM, Shanker V (2019) Solar-light harvesting bimetallic Ag/Au decorated graphene plasmonic system with efficient photoelectrochemical performance for the enhanced water reduction process. ACS Appl Nano Mater 2:4782–4792. https://doi.org/10.1021/acsanm.9b00684
12. Fan M, Lai FJ, Chou HL, Lu WT, Hwang BJ, Brolo AG (2013) Surface-enhanced Raman scattering (SERS) from Au:Ag bimetallic nanoparticles: The effect of the molecular probe. Chem Sci 4:509–515. https://doi.org/10.1039/C2SC21191B
13. Petrikaitė V, Talaikis M, Mikoliūnaitė L, Gkouzi AM, Trusovas R, Skapas M, Niaura G, Stankevičius E (2024) Stability and SERS signal strength of laser-generated gold, silver, and bimetallic nanoparticles at different KCl concentrations. Heliyon 10:2405. https://doi.org/10.1016/j.heliyon.2024.e34815
14. Fathurrohman PZ, Kunarti ES, Wijayanti N, Santosa SJ (2024) Straightforward microwave-assisted synthesis of ultrasmall gold nanoparticles acnhored on reduced graphene oxide for enhanced antibacterial application. Discover Appl Sci 6:311. https://doi.org/10.1007/s42452-024-06002-0
15. Ayareh Z, Moradi M (2022) Nanoplasmonic sensor chip fabricated based on Au nanoparticles: Effect of graphene oxide and reduced graphene oxide. Plasmonics 17:1437–1444. https://doi.org/10.1007/s11468-022-01629-4
16. Mombeshora ET, Muchuweni E (2023) Dynamics of reduced graphene oxide: Synthesis and structural models. RSC Adv 13:17633–17655. https://doi.org/10.1039/D3RA02098C
17. Yu J, Ma Y, Yang C, Zhang H, Liu L, Su J, Gao Y (2018) SERS-active composite based on rGO and Au/Ag core-shell nanorods for analytical applications. Sensors and Actuators B: Chem 254:182–188. https://doi.org/10.1016/j.snb.2017.07.034
18. Zhang X, Cai X, Yin N, Wang Y, Jiao Y, Liu C (2024) Transferable G/Au film for constructing a variety of SERS substrates. Nanomater 14:566. https://doi.org/10.3390/nano14070566
19. Le Ru EC, Auguié B (2024) Enhancement factors: A central concept during 50 years of surface-enhanced Raman spectroscopy. ACS Nano 18:9773–9783. https://doi.org/10.1021/acsnano.4c01474
20. Zheng J, Yang Z, Guo Y, Fang Y (2021) A detailed investigation in the enhancement factor of surface-enhanced Raman scattering in simulation. Plasmonics 16:2207–2214. https://doi.org/10.1007/s11468-021-01442-5
21. Mahmoud MA, Chamanzar M, Adibi A, El-Sayed MA (2012) Effect of the dielectric constant of the surrounding medium and the substrate on the surface plasmon resonance spectrum and sensitivity factors of highly symmetric systems: silver nanocubes. J Am Chem Soc 134:6434–6442. https://doi.org/10.1021/ja300901e
22. Chaffin E, O'Connor RT, Barr J, Huang X, Wang Y (2016) Dependence of SERS enhancement on the chemical composition and structure of Ag/Au hybrid nanoparticles. J Chem Phys 145:054706. https://doi.org/10.1063/1.4960052
23. Suhailin FH, Alwahib AA, Chee HY, Mustafa FH, Hamzah ASA, Zainuddin NH, Omar MF, Razak AAA, Mahdi MA (2022) Fiber-based surface plasmon resonance biosensor for Leptospira DNA detection. IEEE Sensors J 22:20516–20523. https://doi.org/10.1109/JSEN.2022.3207498
24. Kelly KL, Coronado E, Zhao LL, Schatz GC (2003) The optical properties of metal nanoparticles: The influence of size, shape, and dielectric environment. J Phys Chem B 107:668–677. https://doi.org/10.1021/jp026731y
25. He RX, Liang R, Peng P, Zhou Y (2017) Effect of the size of silver nanoparticles on SERS signal enhancement. J Nanoparticle Res 19:267. https://doi.org/10.1007/s11051-017-3953-0
26. Gul M, Kashif M, Muhammad S, Azizi S, Sun H (2025) Various methods of synthesis and applications of gold-based nanomaterials: A detailed review. Crystal Growth & Design 25:2227–2266. https://doi.org/10.1021/acs.cgd.4c01687
27. Mavani K, Shah M (2013) Synthesis of silver nanoparticles by using sodium borohydride as a reducing agent. Conference: Int J Eng Res Technol (IJERT) 2. https://doi.org/10.13140/2.1.3116.8648
28. Razak AAA, Shatar L, Ramli A, Kassim S, Ghazali MSM, Chee HY, Zakaria R, Mahdi MA, Suhailin FH (2024) Surface-enhanced raman spectroscopy (SERS) substrates based on photonic crystal embedded bi-metallic nanoparticles for leptospiral DNA detection. Appl Spectrosc 79:986–996. https://doi.org/10.1177/00037028241303780
29. Alam NS, Sharma N, Kumar L (2017) Synthesis of graphene oxide (GO) by modified hummers method and its thermal reduction to obtain reduced graphene oxide (rGO). Graphene 6:1–18. https://doi.org/10.4236/graphene.2017.61001
30. Rahman L, Shah AHA, Shah A, Salman SM, Jan AK (2022) Synthesis and spectroscopic analysis of Au-Ag alloy nanoparticles with different composition of Au and Ag. Biointerface Res Appl Chem 12:377–390. https://doi.org/10.33263/BRIAC121.377390
31. Hidayah AN, Triyono D, Herbani Y, Saleh R (2022) Liquid surface-enhanced Raman spectroscopy (SERS) sensor-based Au-Ag colloidal nanoparticles for easy and rapid detection of deltamethrin pesticide in brewed tea. Crystals 12:24. https://doi.org/10.3390/cryst12010024
32. Khurana K, Jaggi N (2021) Localized surface plasmonic properties of Au and Ag nanoparticles for sensors: A review. Plasmonics 16:981–999. https://doi.org/10.1007/s11468-021-01381-1

33. Hang Y, Wang A, Wu N (2024) Plasmonic silver and gold nanoparticles: shape- and structure-modulated plasmonic functionality for point-of-caring sensing, bio-imaging and medical therapy. Chem Soc Rev 53:2932–2971. https://doi.org/10.1039/D3CS00793F
34. Saikia M, Dasa T, Saikia BK (2021) A novel rapid synthesis of highly stable silver nanoparticle/carbon quantum dot nanocomposites derived from low-grade coal feedstock. New J Chem 46:309–321. https://doi.org/10.1039/D1NJ04039A
35. Sujitha AS, Saikant R, Ragupathy L, Joe IH, Painuly D (2024) Gold nanoparticles-incorporated electrospun nanofibrous membrane for optical biosensing applications: An experimental and computational approach. Fibers Polym 25:1193–1210. https://doi.org/10.1007/s12221-024-00511-w
36. Zhou H, Wirth R, Gleeson SA, Schreiber A, Mayanna S (2021) Three-dimensional and microstructural fingerprinting of gold nanoparticles at fluid-mineral interfaces. Am Mineralogist 106:97–104. https://doi.org/10.2138/am-2021-7696
37. Ahmed S, Baijal G, Somashekar R, Iyer S, Nayak V (2021) One pot synthesis of PEGylated bimetallic gold–silver nanoparticles for imaging and radiosensitization of oral cancers. Int J Nanomed 16:7103–7121. https://doi.org/10.2147/IJN.S329762
38. Rodwihok C, Wongratanaphisan D, Ngo YLT, Khandelwal M, Hur SH, Chung JS (2019) Effect of GO additive in ZnO/rGO nanocomposites with enhanced photosensitivity and photocatalytic activity. Nanomater 9:1441. https://doi.org/10.3390/nano9101441
39. Calizo I, Balandin AA, Bao W, Miao F, Lau CN (2007) Temperature dependence of the Raman spectra of graphene and graphene multilayers. Nano Lett 7:2645–2649. https://doi.org/10.1021/nl071033g
40. Fathurrohman PZ, Kunarti E, Wijayanti N, Sato N, Amano Y, Machida M, Santosa SJ (2024) A comparative study of the effect of oxygen-containing functional groups in GO and rGO sheets decorated with small gold nanoparticles on bioactivities. J Inorg Organometallic Polym Mater 34:5854–5868. https://doi.org/10.1007/s10904-024-03248-4
41. Chadha N, Sharma R, Saini P (2021) A new insight into the structural modulation of graphene oxide upon chemical reduction probed by Raman spectroscopy and X-ray diffraction. Carbon Lett 31:1125–1131. https://doi.org/10.1007/s42823-021-00234-5
42. Vallés C, Zhang X, Cao J, Lin F, Young RJ, Lombardo A, Ferrari AC, Burk L, Mülhaupt R, Kinloch IA (2019) Graphene/polyelectrolyte layer-by-layer coatings for electromagnetic interference shielding. ACS Appl Nano Mater 2:5272–5281. https://doi.org/10.1021/acsanm.9b01126
43. Shih KY, Kuan YL, Wang ER (2021) One-step microwave-assisted synthesis and visible-light photocatalytic activity enhancement of BioBr/RGO nanocomposites for degradation of methylene blue. Mater 14:4577. https://doi.org/10.3390/ma14164577
44. Shilpa MP, Shetty SJ, Surabhi S, Jeong JR, Morales DV, Murari MS, Bhat VS, Inamdar SR, Ravikirana, Gurumurthy SC (2024) Synthesis, characterization, and FDTD simulations of Ag-enriched rGO nanosheets for catalytic reduction of 4-nitrophenol. J Mater Sci: Mater Electron 35:860. https://doi.org/10.1007/s10854-024-12574-9
45. Gokulakrishnan J, Manojkumar PA, Koppole K (2024) Surfactant-free facile synthesis of Ag/rGO nanohybrid for SERS-based detection of melamine. Plasmonics 19:471–480. https://doi.org/10.1007/s11468-023-01999-3
46. Sengupta I, Sharat Kumar SSS, Pal KS, Chakraborty S (2020) Characterization of structural transformation of graphene oxide to reduced graphene oxide during thermal annealing. J Mater Res 35:1197–1204. https://doi.org/10.1557/jmr.2020.55
47. Huang HH, De Silva KKH, Kumara GRA, Yoshimura M (2018) Structural evolution of hydrothermally derived reduced graphene oxide. Sci Rep 8:6849. https://doi.org/10.1038/s41598-018-25194-1
48. Taratayko A, Kolobova E, Mamontov G (2022) Graphene oxide decorated with Ag and CeO_2 nanoparticles as a catalyst for room-temperature 4-nitrophenol reduction. Catalysts 12:1393. https://doi.org/10.3390/catal12111393
49. De Silva KKH, Huang HH, Joshi RK, Yoshimura M (2017) Chemical reduction of graphene oxide using green reductants. Carbon 119:190–199. https://doi.org/10.1016/j.carbon.2017.04.025
50. De Silva KKH, Huang HH, Yoshimura M (2018) Progress of reduction of graphene oxide by ascorbic acid. Appl Surf Sci 447:338–346. https://doi.org/10.1016/j.apsusc.2018.03.243
51. Yousefimehr F, Jafarirad S, Salehi R, Zakerhamidi SM (2021) Facile fabricating of rGO and Au/rGO nanocomposites using Brassica Oleracea var. Gongylodes biomass for non-invasive approach in cancer therapy. Sci Rep 11:11900. https://doi.org/10.1038/s41598-021-91352-7
52. Kumbhar GS, Patil SV, Sarvalkar PD, Vadanagekar AS, Karvekar OS, Patil SS, Rane MR, Sharma KKK, Kurhe DN, Prasad NR (2022) Synthesis of a Ag/rGO nanocomposite using Bos Taurus indicus urine for nitroarene reduction and biological activity. RSC Adv 12:35598–35612. https://doi.org/10.1039/D2RA06280A
53. Radinović K, Mladenović D, Milikić J, Alsaiari M, Harraz FA, Santos DMF, Paunkovic BS (2022) Tuning electrocatalytic activity of gold silver nanoparticles on reduced graphene oxide for oxygen reduction reaction. J Electrochemical Soc 169:054501. https://doi.org/10.1149/1945-7111/ac67b7
54. Borah B, Dash RK (2022) Improved dielectric properties of rGO/PDMS composites by incorporation of Ag nanoparticles. Journal of Materials Science: Materials Electron 33:12334–12350. https://doi.org/10.1007/s10854-022-08191-z
55. Wu D, Liu Y, Wang Y, Hu L, Ma H, Wang G, Wei Q (2016) Label-free electrochemiluminescent immunosensor for detection of prostate specific antigen based on aminated graphene quantum dots and carboxyl graphene quantum dots. Sci Rep 6:20511. https://doi.org/10.1038/srep20511
56. Goul R, Das S, Liu Q, Xin M, Lu R, Hui R, Wu JZ (2017) Quantitative analysis of surface enhanced Raman spectroscopy of Rhodamine 6G using a composite graphene and plasmonic Au nanoparticle substrate. Carbon 111:386–392. https://doi.org/10.1016/j.carbon.2016.10.019
57. He T, Xiong S, Han H, Wang D, Wang Y, Dai C, Liu W (2023) Facile synthesis of Ag/GO SERS composite with highly sensitive and stable performance. Colloids and Surfaces A: Physicochemical and Engineering Aspects 662:131008. https://doi.org/10.1016/j.colsurfa.2023.131008
58. Liu L, Gao T, Zhao Q, Xue Z, Wu Y (2025) Self-assembled bimetallic plasmonic nanocavity substrate for supersensitive SERS. Optics Laser Technol 181:111827. https://doi.org/10.1016/j.optlastec.2024.111827
59. Zhang CY, Zhao BC, Hao R, Wang Z, Hao YW, Zhao B, Liu YQ (2020) Graphene oxide-highly anisotropic noble metal hybrid systems for intensified surface enhanced Raman scattering and direct capture and sensitive discrimination in PCBs monitoring. J Hazard Mater 385:121510. https://doi.org/10.1016/j.jhazmat.2019.121510
60. Chen Y, Hao J, Yin Z, Wang Q, Zhou Y, Jia L, Li H, Liao W, Liu K (2023) An accuracy improved ratiometric SERS sensor for Rhodamine 6G in Chili powder using a metal–organic framework support. RSC Adv 13:10135–10143. https://doi.org/10.1039/D3RA00790A
61. Augustine S, Saini M, Sooraj KP, Parida BK, Hans S, Pachchigar V, Satpati B, Ranjan M (2023) Au/Ag SERS active substrate for broader wavelength excitation. Optical Mater 135:113319. https://doi.org/10.1016/j.optmat.2022.113319